MODELLISTICA E CALCOLO SCIENTIFICO

MOX

MODELING AND SCIENTIFIC COMPUTING

MOX-Report No. 19/2023

Computational fluid-structure interaction analysis of the end-to-side radio-cephalic arteriovenous fistula

Marcinno', F.; Vergara, C.; Giovannacci, L.; Quarteroni, A.; Prouse, G.

Computational fluid-structure interaction analysis of the end-to-side radio-cephalic arteriovenous fistula

Fabio **Marcinnò**'*[a], Christian **Vergara**[a], Luca **Giovannacci**[b], Alfio **Quarteroni**[c,d] and Giorgio **Prouse**[b]

[a]*LaBS, Dipartimento di Chimica, Materiali e Ingegneria Chimica "Giulio Natta", Politecnico di Milano, Milan, 20133, Italy*
[b]*EOC-Ente Ospedaliero Cantonale, Lugano, 6900, Switzerland*
[c]*MOX, Dipartimento di Matematica, Politecnico di Milano, Milan, 20133, Italy*
[d]*Institute of Mathematics, EPFL, Lausanne, CH-1015, Switzerland, (Professor Emeritus)*

ARTICLE INFO

ABSTRACT

In the current work, we present a fluid-structure interaction study of the end-to-side radio-cephalic arteriovenous fistula. The core of the work consists in simulating different arteriovenous fistula configurations obtained by virtually varying the anastomosis angle, i.e. the angle between the end of the cephalic vein and the side of the radial artery. The mesh used to solve the structural problem takes into account the different thickness and Young's modulus of the vessel walls. In particular, since the aim of the work is to understand the blood dynamics in the very first days after the surgical intervention, the radial artery is considered stiffer and thicker than the cephalic vein. Our results demonstrate that both the diameter of the cephalic vein and the anastomosis angle play a crucial role in order to obtain a regular blood dynamics that could prevent fistula failure. In particular, when a high anastomosis angle is combined with a large diameter of the cephalic vein, the recirculation regions and the low WSS (wall shear stress) zones are reduced. Converesely, from a structural point of view, a low anastomosis angle with a large diameter of the cephalic vein reduce the mechanical stress acting on the vessel walls.

1. Introduction

In the United States in 2019, about 130000 individuals were newly registered as having end stage renal disease (ESRD) which represented an increase of 2.7% from the previous year and 15.8% from a decade ago [48]. ESRD occurs when the kidneys have lost the ability to filter blood [3]. In the majority of the cases, the problem is faced by means of the hemodialysis, which is performed through a mechanical device called dialyser which is able to emulate the function of the kidneys. In order to perform efficiently, the dialyser needs a high blood flow, therefore the creation of an ad-hoc vascular access (VA) becomes mandatory [18].

Nowadays, the most efficient VA available for the hemodialysis is represented by the arteriovenous fistula (AVF) involving a connection between an artery and a vein at the most distal site possible [19, 15]. In particular, the end-to-side radio-cephalic arteriovenous fistula (RCAVF) is the most used technique for VA [47] and it was introduced by Brescia and Cimino, in 1966 [13].

In the RCAVF, the end segment of the cephalic vein is anastomized onto the side of the radial artery, as a consequence the former has to remodel its vessel structure, augmenting the wall thickness and improving its mechanical stiffness due to the increased flow and pressure coming from the systemic circulation. This process is called fistula maturation and it is essential to obtain a stable and trusty vascular access to the vein. Actually, the main problem is represented by the fact that the fistula maturation has a high rate of failure, approximately between 30% and 70% [47, 2]. The failure is due to several complications strongly associated to a non-physiological structural remodelling of the cephalic vein, causing venous intimal hyperplasia (IH) leading to stenosis and thrombosis [18, 35, 20]. Concerning RCAVFs, there are two typical anatomical configurations, with the second situation arising in most of the RCAVFs:

- (Standard-)RCAVF: with 1 inlet (the proximal radial) and 2 outlets (the cephalic vein and the distal radial artery);

- RCAVF-SS: with 2 inlets (the distal and the proximal radial artery) and 1 outlet (the cephalic vein). In this context, blood steal occurs, i.e. a retrograde flow coming from the distal radial artery is generated by the lower resistance of the cephalic vein [47, 18].

The usefulness of the computational methods in hemodynamics has been largely demonstrated in the last 25 years [31, 52], especially in analyzing critical regions such as bifurcations and complex geometric conditions (for example, stenosis or aneurisyms) [8, 51, 41, 43, 44]. Since the disturbed hemodynamics at the anastomosis region, due to the unnatural path and artero-venous mismatch of wall thickness and elestic properties, plays a fundamental role in inducing the cited complications [18], from the first part of the last decade numerical methods have been used to examine in depth the hemodynamics of the AVF.

Concerning the RCAVF-SS case, in [65] the authors propose a FSI in patient specific situations, where both the vessel wall of the radial artery and cephalic vein have the same thickness and stiffness properties. The authors introduce the critical energy loss rate (CEL) referring to the maximum allowable energy loss rate in AVF. In [62], the authors perform a computational fluid dynamics (CFD) study exploiting the Large Eddy Simulation (LES) turbulence model to assess the best anastomosis angle, the one that minimizes oscillating shear index (OSI) and turbulent regions. In [12], the authors, through CFD simulations, compare the impact of an external support device against conventional surgery. They find that the device is able to maintain an optimal anastomosis angle promoting a more regular blood velocity pattern and stable morphology.

Considering FSI studies for the RCAVF case, in [21] the influence of the wall compliance on the hemodynamics of a patient-specific geometry is studied; the numerical results demonstrate that the cephalic vein is subjected to values of WSS two times higher than the healthy level. In [59], the hemodynamics of an idealized geometry is studied, where the artery bed and heel of the AVF seems to be a susceptible area for IH; the authors find abnormal values of the Von-Mises stress at the anastomosis region. In [21, 59], the authors assume different thickness for the vessel walls, and the cephalic vein stiffer than the radial artery, in a situation of already achieved fistula maturation is considered.

Other computational studies are focused on the brachio-cephalic arteriovenous fistula (BCAVF); this configuration has 1 inlet (the proximal brachial artery) and 2 outlets (the distal brachial artery and the cephalic vein). In [19], the results of the FSI are validated against magnetic resonance imaging (MRI) data. A region of high WSS is present at the toe of the anastomosis while a high OSI is found at the heel of the anastomosis. In [46], the BCAVF geometry is reconstructed from 3D ultrasound scan. The authors find very large time-averaged wall shear stresses (TAWSS) at the anastomosis region. In [37], the results of patient-specific FSI are validated against the phase-contrast magnetic resonance angiography (PC-MRA) showing good agreement. In [11], the CFD analysis of the BCAVF is carried out. Thanks to the use of the LES (Large Eddy Simulation) method, it is highlighted that the zone of the anastomosis is characterized by an high-frequency multidirectional disturbed flow. From the same group, in [10] the authors explore the feasibility of coupling a contrast-free MRI protocol with high-resolution computational fluid dynamics (HR-CFD) to relate the hemodynamics changes to vascular wall remodeling occuring during fistula maturation.

In the present work, we propose a pulsatile FSI study for patient-specific end-to-side RCAVF-SS, parametrized on the anastomosis angle, to assess the influence of the latter on hemodynamics and structural quantities, which are relevant for the RCAVF-SS failure. In particular, we study two patients and, by virtually varying the anastomosis angle, we propose three different geometric configurations for each patient. The work focuses on the first days immediately after the surgical intervention, i.e. when the radial artery and the cephalic vein still feature substantial differences in the stiffness and geometric properties. For such reasons, we believe that a FSI simulation is mandatory, since it is able to capture these hetereogenities. According to clinical evidences, in this work the radial artery is much stiffer than the cephalic vein and it has a larger wall thickness.

The novelty of the paper consists in the inclusion of the artero-venous elastic and wall thickness mismatches in a RCAVF-SS FSI study with different anastomosis angles. Moreover, for the first time we focus on the first days after the intervention, which are believed to be the most relevant to determine the condition which may favour the failure [56].

The work is organized as follows. In Sec. 2, we describe the pre-processing for the generation of the fluid and structure grids. In Sec. 3, the mathematical model of the FSI is described. In Sec. 4, we report the input data and we discuss the fluid and structure numerical results. Finally, in Sec. 4.5 and 4.6, we report the conclusions and limitations of our work, respectively.

2. Pre-processing and mesh generation

The geometric reconstructions are obtained from Echo-Color Doppler (ECD) acquisitions given by the EOC - Ente Ospedaliero Cantonale, Lugano, Switzerland, in particular at the Divisions of Vascular Surgery and Angiology. All the data are treated under the patients' consent. The 3D lumen surfaces were taken from a previous CFD work of the group, see [62].

In this work, we study two patients by means of a FSI computational study, referred in what follows to as P1 and P2, who underwent fashioning of end-to-side radio-cephalic vascular access with angles equal to 40° and 70°, respectively. Then, we virtually vary the anastomosis angle and we analyze three different geometric configurations for each patient: 20°, 40°, 60° for P1 ($P1 - 20$, $P1 - 40$, $P1 - 60$) and 30°, 50°, 70° for P2 ($P2 - 30$, $P2 - 50$, $P2 - 70$). For the sake of clearness, in Fig.1, we report, for a generic angle ϑ, the configurations for P1 and P2. The arterial tracts considered for P1 and P2 are 160 mm and 165 mm long, respectively; the anastomosis region (i.e. where the vein is sawn to the artery) has a length in the range of 15-20 mm, see Figure 2, above, blue region.
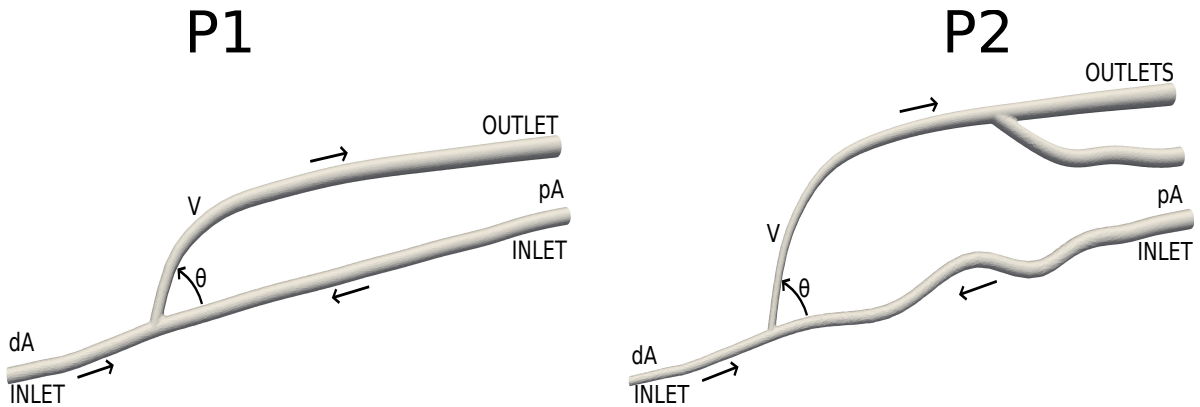
Figure 1: Computational geometry for a generic anastomosis angle ϑ of P1 (left) and P2 (right). The arrows indicate the direction of the blood flow. pA= proximal artery, dA= distal artery, V= vein.

The generation of the tetrahedral computational meshes is achieved by means of the Vascular Modeling Toolkit (VMTK) [5]. In particular, the fluid mesh is obtained starting from the 3D reconstructed lumen surfaces with an average space discretization parameter $h = 0.6$ mm, with a boundary layer (BL) composed of three heterogeneous layers, where the one nearest to the wall has a thickness of 0.12 mm; the dimension of the other two internal layers increases by a factor of 25% with respect to the previous one. The structure mesh is generated by means of an extrusion of the 3D fluid mesh through the combined use of VMTK, MATLAB [45], and Gmsh [36]; it is composed of three layers with a total thickness of 0.1 mm (cephalic vein) and 0.3 mm (radial artery) each, and it is conforming at the interface to the fluid one [29].

In the top of Fig.2, we report for each patient the structure meshes in the three configurations. We also highlight by different colours the arterial and vein regions. Indeed, it is worth pointing out that in this work we use two different Young's modulus E for the radial artery and cephalic vein to account for their different elastic properties. In particular, since we are interested in studying the fluid-structural conditions in the first hours after the operation, we set the artery stiffer than the vein; moreover, we also geometrically differentiate the vein and the artery by accounting for their different wall thickness τ. The value of the Poisson's coefficient ν are equal for both the vessels.

3. Numerical Methods

3.1. The fluid-structure interaction problem

The fluid dynamics is modeled by means of the incompressible homogeneus Navier-Stokes equations written in the arbitrary Lagrangian-Eulerian (ALE) formulation. The dynamics of the vessel wall is modeled through the linear elasticity equations written in a Lagrangian framework. This is justified upon noticing that AVF experiences small
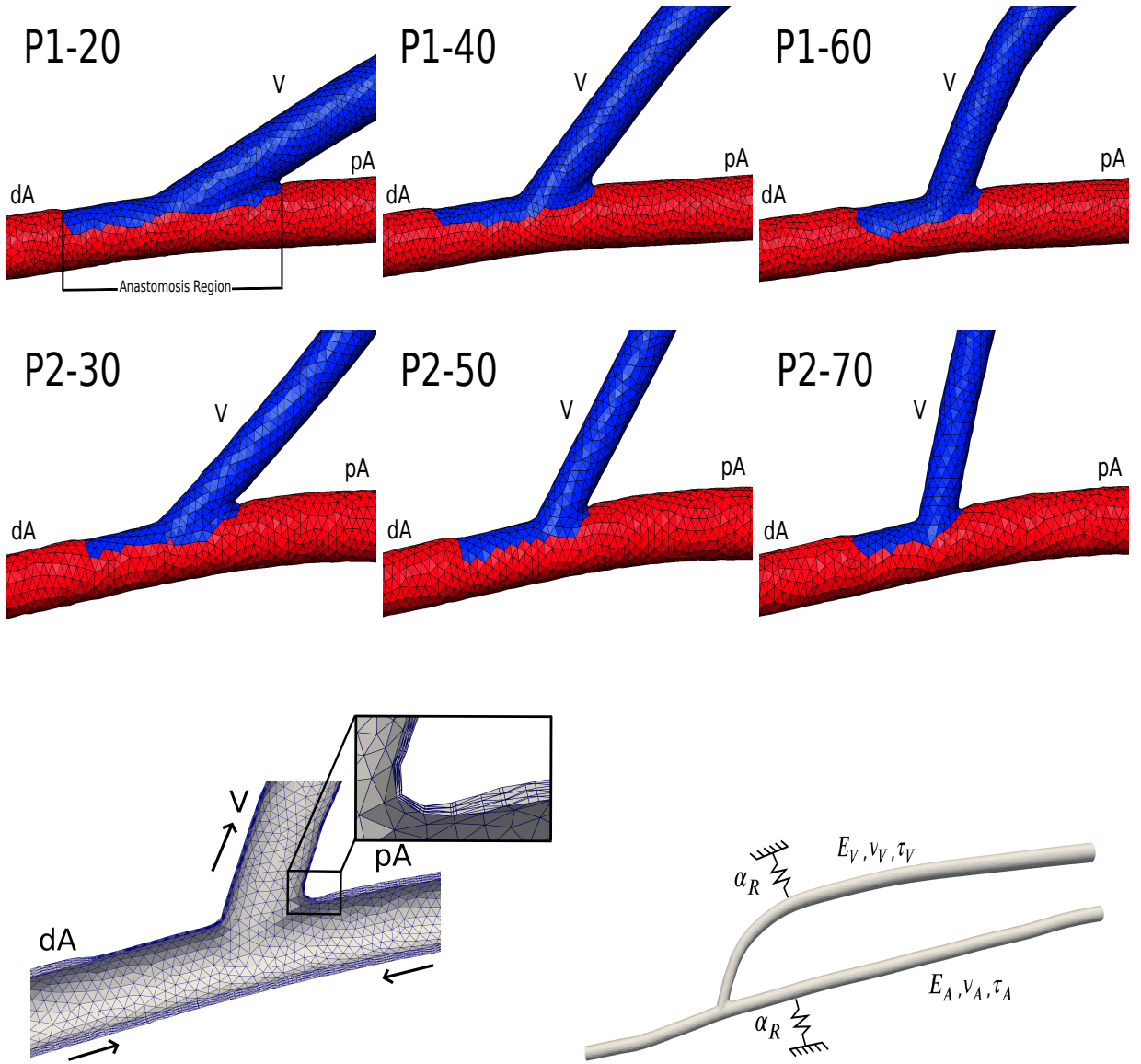
Figure 2: Top: Computational structure meshes. The blue region represents the cephalic vein while the red one the radial artery. Bottom-Left: Longitudinal section of the structure mesh ($P1 - 60$). The thickness discontinuity between the radial artery and the cephalic vein is visible. The arrows indicate the blood flow's direction. Bottom-Right: Structural parameters. E_A is the artery Young's modulus, E_V the vein Young's modulus, ν_A the artery Poisson's coefficient, ν_V the vein Poisson's coefficient, τ_A and τ_V the thickness of the artery and vein walls, respectively, α_R the Robin surrounding tissue coefficient. pA= proximal artery, dA= distal artery, V= vein.

vessel wall displacements to their reference configuration [46, 19]. For the sake of notation, from now on, the quantities written in a pure Lagrangian framework (reference configuration) are denoted with $\hat{\cdot}$. In this respect, we introduce a fluid mesh motion $\mathbf{d}_F$, solution of a harmonic extension within the lumen of the boundary displacement. This allows us to move the fluid mesh as follows

$$\mathbf{x}(t) = \hat{\mathbf{x}} + \hat{\mathbf{d}}_F(\hat{\mathbf{x}}, t) \qquad \forall \hat{\mathbf{x}} \in \hat{\Omega}_F .$$

Referring to Fig.3, let $\Omega_F(t)$ and $\hat{\Omega}_S$ be the fluid and structure domains, respectively, and $\Sigma(t)$ the interface between the fluid and the structure domains. Let $\mathbf{u}(\mathbf{x}, t) : \Omega_F(t) \to \mathbb{R}^3$ the fluid velocity, $p(\mathbf{x}, t) : \Omega_F(t) \to \mathbb{R}$ the fluid pressure,

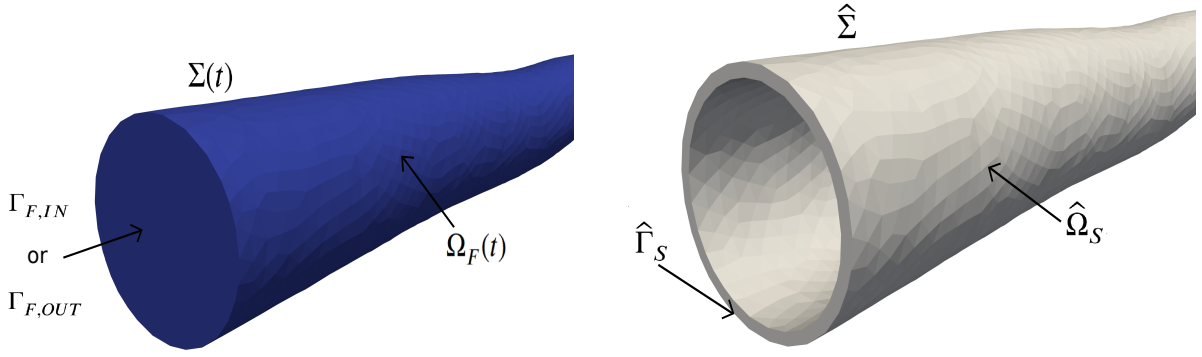**Figure 3:** Left: Fluid domain. Right: Structure domain.

$\widehat{\mathbf{d}}(\mathbf{x}, t) : \widehat{\Omega}_S \rightarrow \mathbb{R}^3$ the displacement of the vessel walls, and $\mathbf{u}_F$ the velocity of the fluid mesh. In the following, we report the formulation of the FSI problem:

For any $t > 0$, find $\mathbf{u}$, p, $\widehat{\mathbf{d}}$, such that:

$$\rho_F \frac{\partial \mathbf{u}}{\partial t} + \rho_F((\mathbf{u} - \mathbf{u}_F) \cdot \nabla)\mathbf{u} - \nabla \cdot T_F(\mathbf{u}, p) = \mathbf{0} \qquad \text{in} \quad \Omega_F(t), \tag{1a}$$

$$\nabla \cdot \mathbf{u} = 0 \qquad \text{in} \quad \Omega_F(t), \tag{1b}$$

$$\mathbf{u} = \frac{\partial \mathbf{d}}{\partial \mathbf{t}} \qquad \text{on} \quad \Sigma(t), \tag{1c}$$

$$T_F(\mathbf{u}, p)\mathbf{n} = T_S(\mathbf{d})\mathbf{n} \qquad \text{on} \quad \Sigma(t), \tag{1d}$$

$$\rho_S \frac{\partial^2 \widehat{\mathbf{d}}}{\partial t} - \nabla \cdot \widehat{T}_S(\widehat{\mathbf{d}}) = \mathbf{0} \qquad \text{on} \quad \widehat{\Omega}_S, \tag{1e}$$

$$-\Delta \widehat{\mathbf{d}_F} = \mathbf{0} \qquad \text{on} \quad \widehat{\Omega}_F, \tag{1f}$$

$$\widehat{\mathbf{d}}_F = \widehat{\mathbf{d}} \qquad \text{on} \quad \widehat{\Sigma}, \tag{1g}$$

with suitable initial conditions on $\mathbf{u}$, $\widehat{\mathbf{d}}$, $\dot{\widehat{\mathbf{d}}}$ and where ρ_F and ρ_S are the fluid and structure densities. Equations (1c) and (1d) represent the interface conditions stating the continuity of fluid and structure velocities and forces. Problem (1) needs to be equipped with suitable boundary conditions which will be detailed in the next section. Notice that $\mathbf{u}_F = \dot{\mathbf{d}}_F$, $T_F(\mathbf{u}, p) = -pI + \mu_F(\nabla \mathbf{u} + \nabla \mathbf{u}^T)$ is the fluid Cauchy stress tensor with μ_F the fluid dynamic viscosity, $\widehat{T}_S(\widehat{\mathbf{d}}) = \lambda \nabla \cdot \widehat{\mathbf{d}}I + \mu_S(\nabla \widehat{\mathbf{d}} + \nabla \widehat{\mathbf{d}}^T)$ is the structure Piola-Kirchhoff stress tensor. It is worth noting that $\lambda = \dfrac{E\nu}{(1 + \nu)(1 - 2\nu)}$ and $\mu_S = \dfrac{E}{2(1 + \nu)}$ are the Lamé constants, where ν is the Poisson's coefficient.

The time discretization is obtained by means of a second order backward differentiation formula[34] (BDF2), for both fluid and structure problems [49]. The FSI system is linearized thanks to the inexact Newton method, in particular neglecting shape derivatives in the Jacobian matrix. The problem is solved monolithically by using a block preconditioner based on the SIMPLE preconditioner for the fluid subproblem [23] and by means of the GMRES method with an absolute tolerance of 10^{-10}. It is worth noting that the geometry problem (see (1f) and (1g)) is treated implicitly, i.e. at every Newton subiteration the fluid mesh is moved accordingly to the harmonic motion.

The space discretization of the Navier-Stokes equations is obtained using piecewise linear Finite Elements ($\mathbb{P}1-\mathbb{P}1$) for both the velocity and pressure, stabilized by means of the SUPG-PSPG method [63], which allows also to control the advection dominated regime. The elasto-dynamics problem is discretized using $\mathbb{P}1$ Finite Elements.

3.2. Boundary conditions

Fluid outlet boundary conditions are imposed by means of an absorbing resistance R_a [49]:

$$R_a = \sqrt{\frac{\rho_f \beta}{2}} \frac{1}{A_F^{\frac{3}{4}}}, \quad \beta = \frac{E\tau\pi}{(1-\nu^2)A_F}, \quad \tau = \sqrt{\frac{A_F + A_S}{\pi}} - \sqrt{\frac{A_F}{\pi}},$$

where A_F is the area of the fluid outlet boundary and A_S is the area of the outlet surface of the structure. Therefore, assuming a constant normal traction on $\Gamma_{F,OUT}$, the outlet fluid condition is defined as

$$T_F(\mathbf{u}, p)\mathbf{n} \cdot \mathbf{n} = R_a * \int_{\Gamma_{F,OUT}} \mathbf{u} \cdot \mathbf{n} \, d\gamma + P_{EXT} \quad \text{on} \quad \Gamma_{F,OUT},$$

where P_{EXT} is the external pressure and with homogeneous tangential traction conditions [32]. Regarding the inlet, we enforce a Dirichlet condition by considering a parabolic velocity profile:

$$\mathbf{u}(\mathbf{x}, t) = -\frac{Q_{IN}}{A_F \rho_F}\left(1 - \frac{r^2}{R^2}\right)\mathbf{n} \quad \text{on} \quad \Gamma_{F,IN},$$

where Q_{IN} is the prescribed flow rate taken from [62], plotted in Fig.4 . It is worth noting that the values are those typical of a non-mature fistula and in agreement with the literature [12].
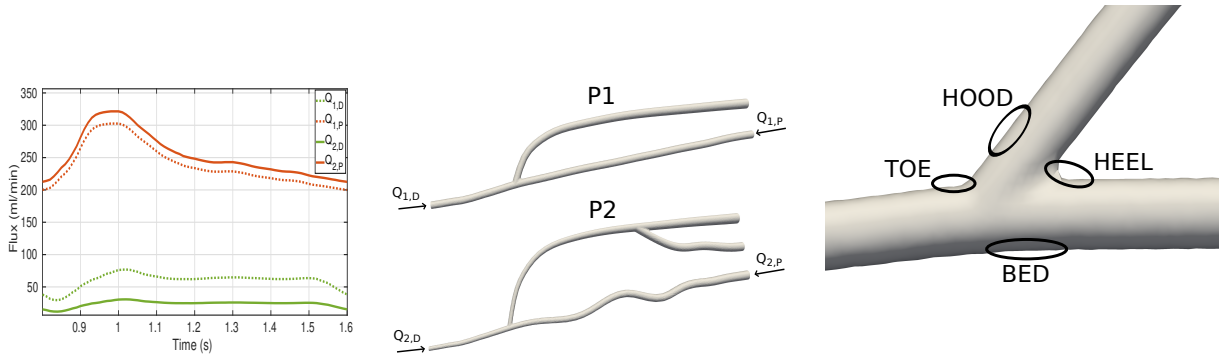
Figure 4: Inlet flow rates (left), computational domains (middle) and zones of clinical relevance at the anastomosis region (right).

Concerning the structure problem, since both the inlet and outlet boundaries are far enough from the zone of hemodynamics interest, i.e. the anastomosis region, the boundary conditions for the vessel displacement are imposed through a zero-displacement constrain on both the axial and radial directions:

$$\hat{\mathbf{d}} = \mathbf{0} \quad \text{on} \quad \hat{\Gamma}_S.$$

Moreover, in order to reliably simulate the displacement of the vessels, we model the presence of the surrounding tissue around the vein and the artery by means of the following Robin condition on the external surface $\hat{\Gamma}_{EXT}$ [53]:

$$\alpha_R \hat{\mathbf{d}} + \hat{T}_S(\hat{\mathbf{d}})\mathbf{n} = P_{EXT} \quad \text{on} \quad \hat{\Gamma}_{EXT}, \tag{2}$$

where α_R is the elastic coefficient of the surrounding tissue.

4. Results & Discussion

In this section, we report the obtained numerical results on the parameteric configurations of the two end-to-side RCAVF-SS patients. The results are showed through the following outline. In Sec.4.1, we describe the hemodynamics and structure quantites of interest. In Sec.4.2, we detail the input data and other details of the FSI simulations. In Sec.4.3, we discuss the numerical results concerning the hemodynamics quantities, whereas in Sec.4.4 the outcomes related to the structure quantities.

4.1. Relevant hemodynamics quantites

Concerning the hemodynamics, we are interested into the following quantities:

- The velocity and pressure distribution at the anastomosis region. Indeed, disturbed flow, abnormal recirculation regions and elevated pressure may provoke conditions favouring intimal hyperplasia (IH) [37];

- The Wall Shear Stress (WSS). It is the magnitude of a vector quantity representing the tangential shear stress caused by the fluid flowing on the vessel wall:

$$WSS = \sigma_F \mathbf{n} - (\sigma_F \mathbf{n} \cdot \mathbf{n})\mathbf{n}.$$

In the systemic arterial context, a normal WSS is considered between $1 - 7$ Pa. In particular, small (< 1 Pa) and oscillatory values are strictly connected to the cardiovascular complications such as IH and stenosis. On the other hand, high WSS (> 7 Pa) protects against IH, but it may provoke endothelial cell cleavage and induce thrombosis [26]. As stated in [14], the constant presence of high WSS may result in VA dysfunction;

- The Oscillatory Shear Index (OSI). It is a scalar quantity representing the degree of shear reversal in a pulsatile flow; it goes from 0 in a uni-directional flow to 0.5 in a reversing flow with no mean shear direction [4]; elevated values of OSI, that is high oscillatory WSS, favour the conditions that could lead to stenosis triggering venous IH [26, 27, 57, 16]. Let us define T as the final time of the simulation, the OSI is defined as follows:

$$OSI(\mathbf{x}) = \frac{1}{2} \left[1 - \frac{|| \int_0^T \mathbf{WSS}(t, \mathbf{x}) \, dt ||}{\int_0^T ||\mathbf{WSS}(t, \mathbf{x})|| \, dt} \right] ;$$

- Time Averaged Wall Shear Stress (TAWSS). It is a scalar quantity measuring the time-average shear. Fixed a space location, the TAWSS is defined as:

$$TAWSS(\mathbf{x}) = \frac{1}{T} \int_0^T ||\mathbf{WSS}(t, \mathbf{x})|| \, dt.$$

Small TAWSS values could bring to IH formation and stenosis [16]. In [12], the authors find that regions with high OSI are associated by low TAWSS in the AVF context.

Concerning the structure variables, we are interested into:

- Displacement of the vessel walls. Since the vessel dilation is necessary in order to obtain the requested flow rate by the dialyser [38], we aim to understand which is the role of the vessel displacement in the context of fistula maturation. In particular, since there is no information in literature, we want to establish which is the correlation between the displacement of the cephalic vein with the non-correct maturation of the juxta-anastomotic region;

- Von Mises stress. It is one of the most used criteria for checking yield conditions [1, 58]. We are interested in computing which parts of the vessel walls are subjected to a large mechanical stress, to understand if a correlation between the high stress zones and VA failure can be stated. Considering σ as the Cauchy stress tensor corresponding to T_S, the Von Mises stress is defined as follows:

$$\sigma_v = \frac{1}{2} \left[(\sigma_{11}^2 - \sigma_{22}^2) + (\sigma_{22}^2 - \sigma_{33}^2) + (\sigma_{33}^2 - \sigma_{11}^2) + (\sigma_{12}^2 - \sigma_{13}^2) + (\sigma_{23}^2) \right].$$

For the analysis of these quantities, we often refer to specific regions of the fistula of clinical relevance, since they are considered crucial for the study of stenosis due to IH and of thrombosis at the anastomosis, see Fig. 4, right.

4.2. Numerical setting of the simulations

In the following, we report some details of the numerical discretization and data of the FSI problem. The numerical results are obtained by means of the LifeV [23, 24, 33, 22] Finite Element library for the approximation of Partial Differential Equations by the Finite Elements Method. The software has been developed at Ecole Polytechnique Fédérale de Lausanne, MOX laboratory at Politecnico di Milano, INRIA-Paris, and Emory University [9]. The numerical simulations were run at MOX laboratory clusters on 4 processors Xeon E5-4610 having a total of 56 cores and RAM of 504 GB.

In order to numerically solve the FSI problem, we introduce a uniform time discretization in which Δt is the step size and T is the heartbeat period. In all the numerical experiments, we set $\Delta t = 10^{-3} s$ and $T = 0.8 s$.

The density and the dynamic viscosity of the blood are $\rho_F = 1.060 \, g/cm^3$ and $\mu_F = 0.035 \, g/(cm \cdot s)$. The cephalic vein and the radial artery are assumed to have the same density $\rho_S = 1.2 \, g/cm^3$; moreover, we assume that the two patients have the same mechanical properties.

Concerning the elastic properties, we set the artery stiffer than the vein, i.e. $E_A = 2.5$ MPa (suitable literature range 2.68 ± 1.68 MPa) [42] and $E_V = 0.5$ MPa (suitable literature range 0.45 ± 0.05 MPa) [55], respectively; moreover, we impose the same Poisson's coefficient $\nu_V = \nu_A = 0.45$ [61, 6] and elastic surrounding tissue coefficient $\alpha_R = 2.5 \times 10^6 \frac{Pa}{cm}$ (see Eq. 3.2) for both the radial artery and the cephalic vein. Such values have been properly calibrated in order to obtain physiological displacements coherent to the literature. Regarding the thickness of the vessel walls, we use $\tau_V = 0.1$ mm (suitable literature range 0.425 ± 0.375 mm) [64] for the cephalic vein and $\tau_A = 0.3$ mm (suitable literature range 0.28 ± 0.05 mm) [42, 39] for the radial artery.

It is worth pointing out that we discard the first heartbeat in order to obtain numerical results at regime conditions and focus our analysis on the second one.

4.3. Blood dynamics analysis

In this section, we aim to analyze the numerial results concerning the fluid dynamics.

In Fig.5, we report the velocity field on a longitudinal slide at two representative instants (systolic peak $t = 1.0$ and deceleration phase $t = 1.3$ s), for P1 and P2.

In Fig. 6, we describe the pressure field of the anastomosis region at the systolic peak ($t = 1.0$) for P1 and P2.

In Fig. 7, in the first and second row, we report the TAWSS for P1 and P2, respectively; while, in Fig. 8, we evalute the OSI, reporting the top and bottom view of the cephalic vein for P2.

In Fig. 9, we report the space-averaged WSS at specific regions in the toe, hood, heel and bed of the anastomosis for P1 and P2 at every instants of the cardiac cycle.

4.3.1. Comments to fluid results

Regarding P1, and considering the velocity field (Fig. 5), we notice the creation of a huge vortex at the toe of the anastomosis (left part of the anastomosis) and a little vortex at the heel (right-upper part of the anastomosis) of the anastomosis. Coherently, passing from the systolic peak to the deceleration phase, the magnitude and the dimension of the main vortex decrease; it is worth noting that the deceleration of the flow does not cause any further abnormal recirculation region and for the entire cardiac cycle the toe of the anastomosis is subjected to the action of the vortex. We believe that since the AVF is far from the heart, it is less affected by the passage towards the different phases of the cardiac cycle, and there is no vortex dissipation at the anastomosis region. The intensity and the shape of the vortex change by varying the anastomosis angle; in particular, we notice that P1-20 appears to be the configuration which induces more disturbed flow; on the other hand, P1-60 is the most conservative configuration leading to a less chaotic condition. Regarding P2, we do not see relevant differences in the vortex dimension and velocity magnitude between the two different istants of the cardiac cycle. Moreover, differently from P1, there are no changes in the blood dynamics pattern when varying of the anastomosis angle. We believe that the main reason behind the fact that, unlike P1, the vortex at the center of the anastomosis of P2 does not decrease its dimension when the anastomosis angle increases is due to the fact that the diameter of the cephalic vein, which is too small in comparison to the radial artery. In Tab. 1, we report the diameters of the cephalic vein and radial artery of P1 and P2 to highlight the correlation with the disturbed flow.

In [40], the authors state that a cephalic vein diameter below 2 mm and a diameter of the radial artery below 1.5 mm could play a crucial role in fistula failure. In [7] and [66], the authors find that in order to favour fistula maturation, the diameter of the cephalic vein should be at least of 2.5 mm. This is confirmed by our results since with
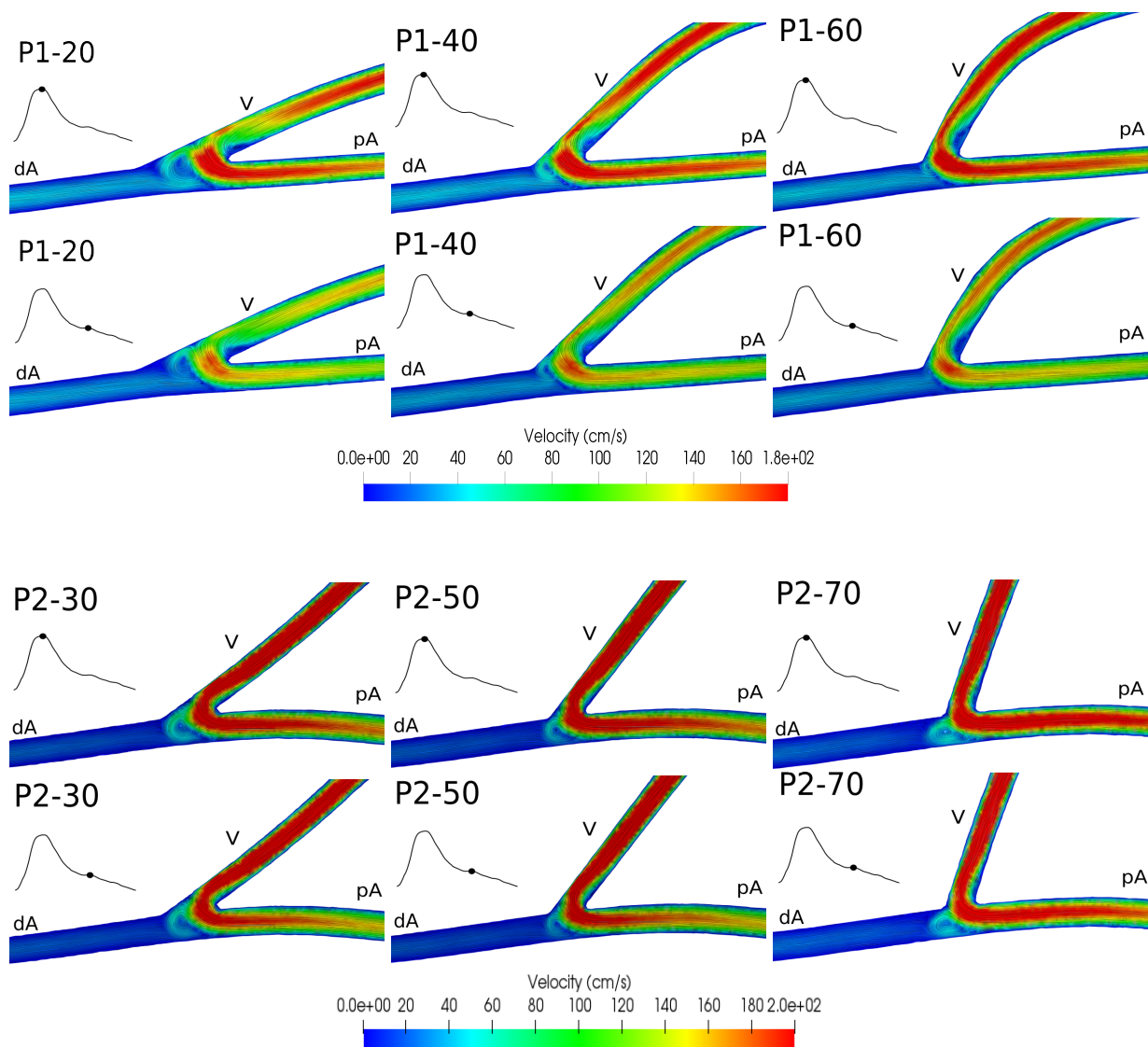
Figure 5: Velocity field at the anastomosis region. First Row: P1 at the systolic peak ($t = 1s$) is reported. Second Row: P1 at the deceleration phase ($t = 1.3s$) is reported. Third Row: P2 at the systolic peak ($t = 1s$) is reported. Fourth Row: P2 at the deceleration phase ($t = 1.3s$) is reported. pA= proximal artery, dA= distal artery, V= vein

P2 (diameter of the cephalic vein smaller than 2.5 mm) we observe the presence of a vortex that leads to a disturbed flow independently of the anastomosis angle. Instead, in P1 (diameter of the cephalic vein larger than 2.5 mm), we have that, if the anastomosis angle is large enough, the vortex disappears and the flow becomes more regular. Therefore, we suggest that both the anastomosis angle and the diameter of the vessels could play a fundamental role in avoiding the generation of disturbed flow and thus in fistula maturation. Notice that the values of the velocity magnitude are coherent with other works [17, 25] and with experimental measures [30].

From Fig. 6 we observe that for both the patients, the highest value of the pressure is registered between the toe and the hood. This is coherent with the velocity field, since at these locations there is a stagnation point, due to the high flow rate coming from the proximal radial artery which goes perpendicular to the cephalic vein walls. The pressure field along the anastomosis region has the same pattern in all the six configurations, but with different magnitude. It is known that in healthy patients, the cephalic vein has pressures of about 7-15 mmHg [50]; since in the AVF the cephalic vein is connected with the systemic arterial network, coherently its pressure increases suddenly. In P1, where the diameter of the vessels is similar and, in particular, the cephalic vein diameter is larger than the radial artery diameter (see Tab.
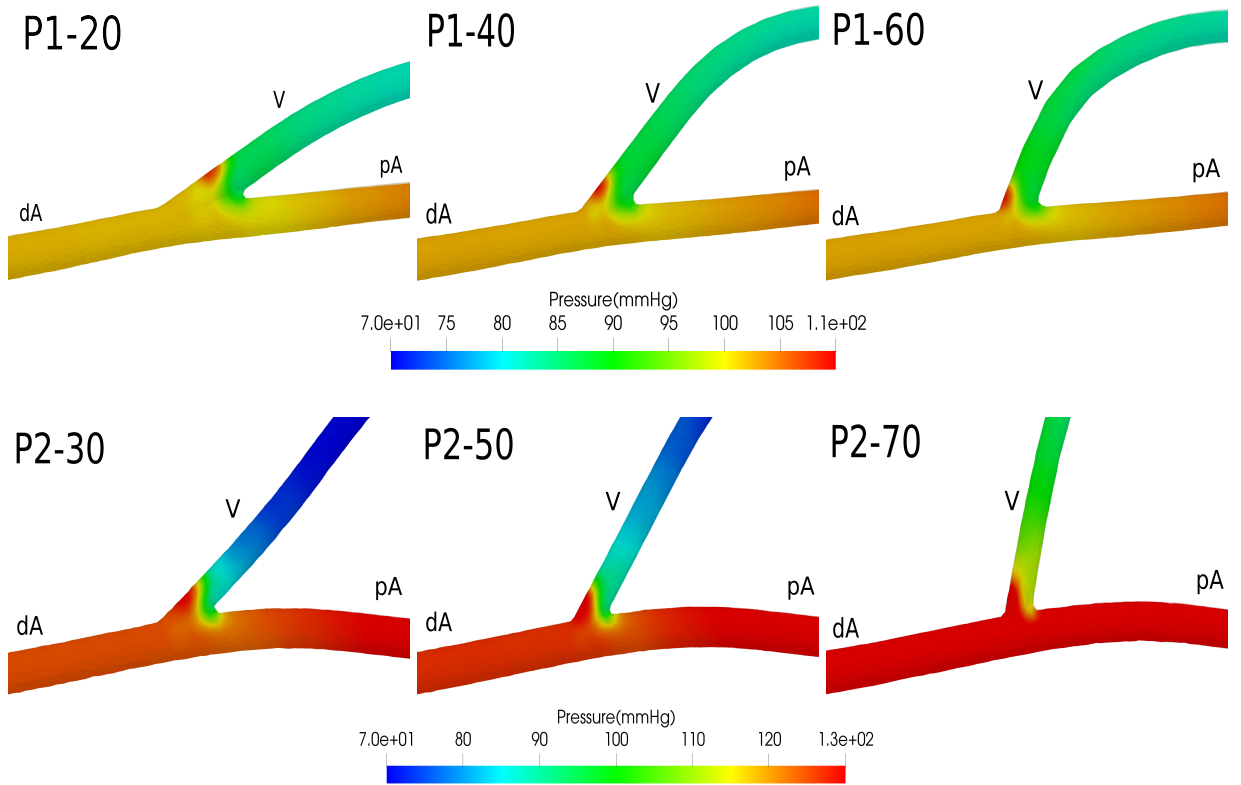
Figure 6: Pressure field at the anastomosis region. First row: P1 configurations at the systolic peak ($t = 1s$). Second row: P2 configurations at the systolic peak ($t = 1s$). pA= proximal artery, dA= distal artery, V= vein. Notice the different scales used for the two patients, in order to highlight differences among anastomosis angles.

Table 1
Diameter of the cephalic vein (D_c) and radial artery (D_r) for P1 and P2.

	P1	P2
D_r	2.85 mm	2.28 mm
D_c	3.03 mm	2.05 mm
$\frac{|(D_c - D_r)|}{D_r} * 100$	6.3 %	11.2 %

1), the pressure inside the cephalic vein is almost equal in all the three configurations, reaching a value of the blood pressure close to that of the systemic arterial circulation. In P2, we think that the small diameter of the cephalic vein causes a small pressure along the cephalic vein (and as a consequence an increase of the velocity field, see the last two rows of Fig. 5) making the dilation of the cephalic vein more difficult.

Regarding the TAWSS, in Fig. 7, for all the configurations, we note that the distal part of both the radial artery and cephalic vein are less subjected to the action of the shear stress making them susceptible zones for the creation of IH and stenosis. The values and the regions of high and low TAWSS are in agreement with [17]. The variation of the anastomosis angle and the cephalic vein diameter do not seem to have any effect on the WSS at the distal part of the radial artery, while an increase of the anastomosis angle causes an increase of the TAWSS at the proximal and distal part of the cephalic vein. In the clinal literature, it is well know that the juxta-anastomotic region (i.e. the proximal part of the cephalic vein) is at high risk for stenosis [54], therefore since the augmenting of the anastomosis angle causes an increasing of the TAWSS in the proximal part of the cephalic vein, we believe that P1-60 and P2-70 are the best configuration for the protection from stenosis, indepently of the cephalic vein diameter. It is worth noting that the
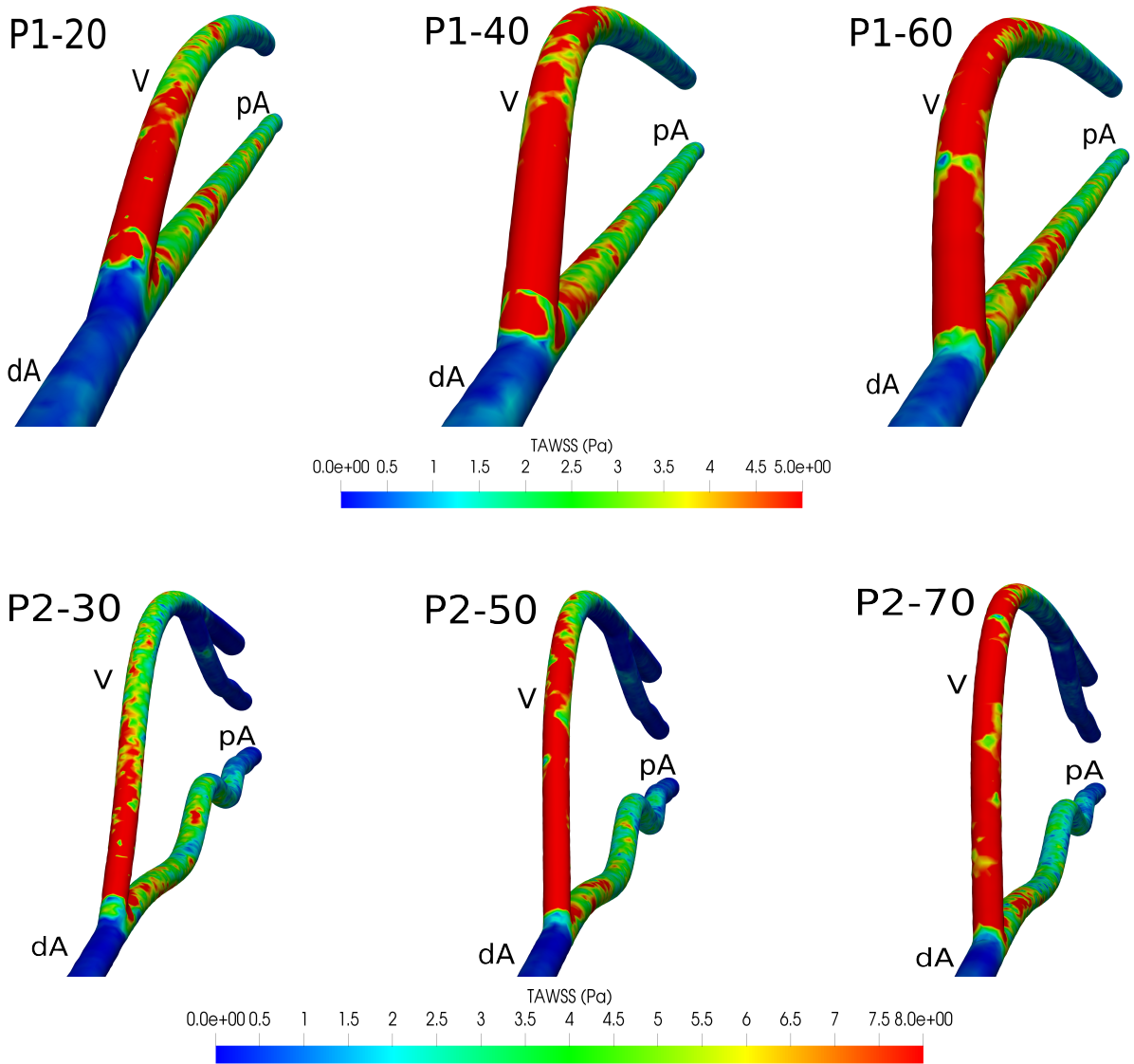
Figure 7: First Row: TAWSS of P1. Second Row: TAWSS of P2. pA = proximal artery, dA = distal artery, V = vein. Notice the different scales used for the two patients, in order to highlight differences among anastomosis angles.

small diameter of the cephalic vein causes a decrease of pressure along the cephalic vein (see Fig. 6), but on the other hand it generates an increase of the velocity field, i.e. an increase of the TAWSS (which should be better in order to avoid the stenosis).

In Fig. 8, the OSI is analyzed, in particular we focus on the distal part of the cephalic vein of P2. The bifurcation at the distal part of the cephalic vein generates an anomoulus pattern of the OSI in both the top and bottom part of the vein. P2-30 and P2-50 seem to be the worst scenario generating an extremely high oscillatory shear stress. P2-70 is more conservative, especially in the bottom part of the cephalic vein. About OSI, our numerical results are in agreement with [17]. It is worth remembering that the only parameter changing between the three configurations of P2 is the anastomosis angle, therefore we believe should exist a strong relation between the generation of the stenosis in the distal part of cephalic vein and the anastomosis angle. In accordance with [28], the distal part of the cephalic vein is one of the most affect sited of stenosis; here, we coherently experiment low value of WSS and high OSI. As stated in [60], after and before bifurcations or branches, there is the production of flow disturbances and regions of flow separation, in which the OSI can increase creating at the distal part of the cephalic vein the perfect condition
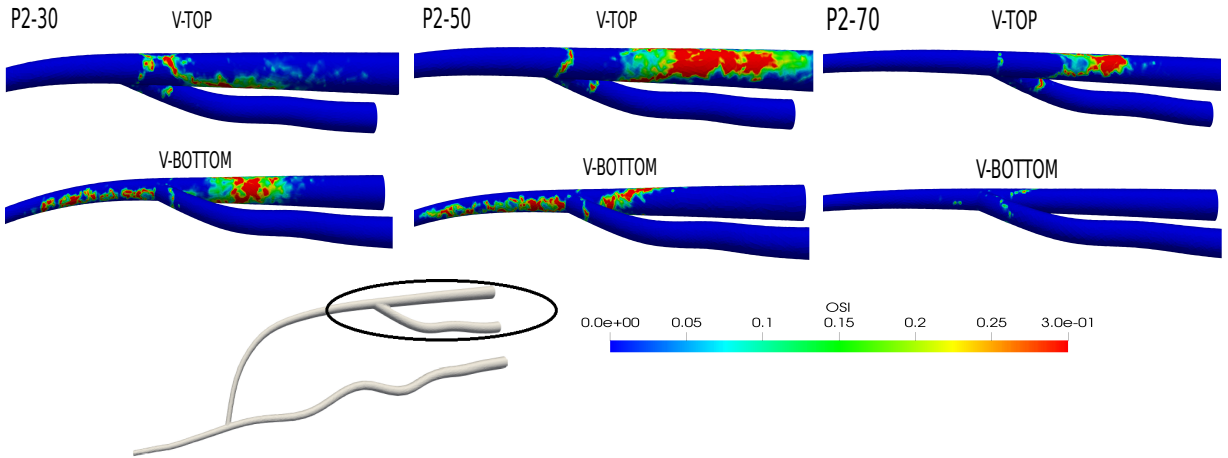
Figure 8: P2. OSI at the distal part of the vein, represented in the circle. V-TOP = vein top view. V-BOTTOM = vein bottom view.

for the stenosis development. We do not report OSI values for P1 since we encounter a quasi-zero value along all the arteriovenous fistula except at the toe of the anastomosis of P1-20, but we consider those values extremely low and not of clinical relevance. It is worth pointing out that our FSI results show a complete different OSI pattern with respect to the rigid study [62], where the largest OSI values were found near to the anastomosis region, whereas in our case in the distal part of the vein.

Considering the WSS along time in specific locations (see Fig. 9), it is worth highlighting that except for P2-HOOD and P2-HEEL, we observe that the configurations with the lowest angles (P1-20 and P2-30) generate the lowest WSS. Regarding the toe, both P1 and P2 experience very low shear stress, in particular the conditions which seems to better protect the toe of the anastomosis are those represented by the angles P1-40 and P2-70, but in general, all the six configurations are characterized by low WSS. We note that the WSS has an oscillant-in-time behavior until the systolic peak, in particular, P1 has the highest oscillations. Looking at the bed, we see that P2 again is characterized by higher WSS values and P1 has a relevant oscillanting-in-time behaviour before the sytolic peak. Also for the bed of the anastomosis, the low angle configurations (P1-20,P1-40,P2-30,P2-50) show lower value of shear stress, while P1-60 and in particular P2-70 have normal values guranteeing a better protection against the IH. It is worth noting that the bed of the anastomosis is another typical sites for the creation of the stenosis [60]. Considering that in AVF context, a healthy WSS is below 7 Pa, at the heel of the anastomosis we encounter comparable values to that of the healthy condition. In particular concerning P1, P1-40 at the systolic peak reaches the healthy limit, while P1-20 and P1-60 are extensively under the limit. Referring to P2, P2-70 seems the best configuration while P2-30 and P2-50 exceed the healthy WSS limit practically in all the phases of the cardiac cycle. Finally, we look at the hood of the anastomosis which can be considered part of the juxta-anastomotic region. Here, the values of the WSS are extremely high for all the configurations. Looking to P1, the anastomosis angle has a very small effect in the changing of the values of WSS, while in P2 the best condition is P2-70 which is able to mantain the value of WSS at the lowest level possible. In general, P2 has higher value of the WSS in all the regions, we belive that this condition is due to higher velocites obtained.

4.4. Structural analysis results

In this section, we present the numerical results concerning the vessel wall structural quantities.

In Fig.10, we report, by means of a longitudinal slice, the displacement magnitude of the anastomosis region at the systolic peak ($t = 1s$) for P1 and P2. In Fig. 11, we evaluate the space-averaged Von Mises stress at heel, bed, hood and toe of the anastomosis for P1 and P2, respectively.

4.4.1. Comments to structure results

Referring to displacement field, in Fig.10, we observe two opposite trends for P1 and P2. In particular, in the former, an increase of the anastomosis angle generates a decrease of the displacement magnitude at the anastomosis region (between the toe and the floor) and an increase of the displacement along the juxta-anastomotic region. Instead,
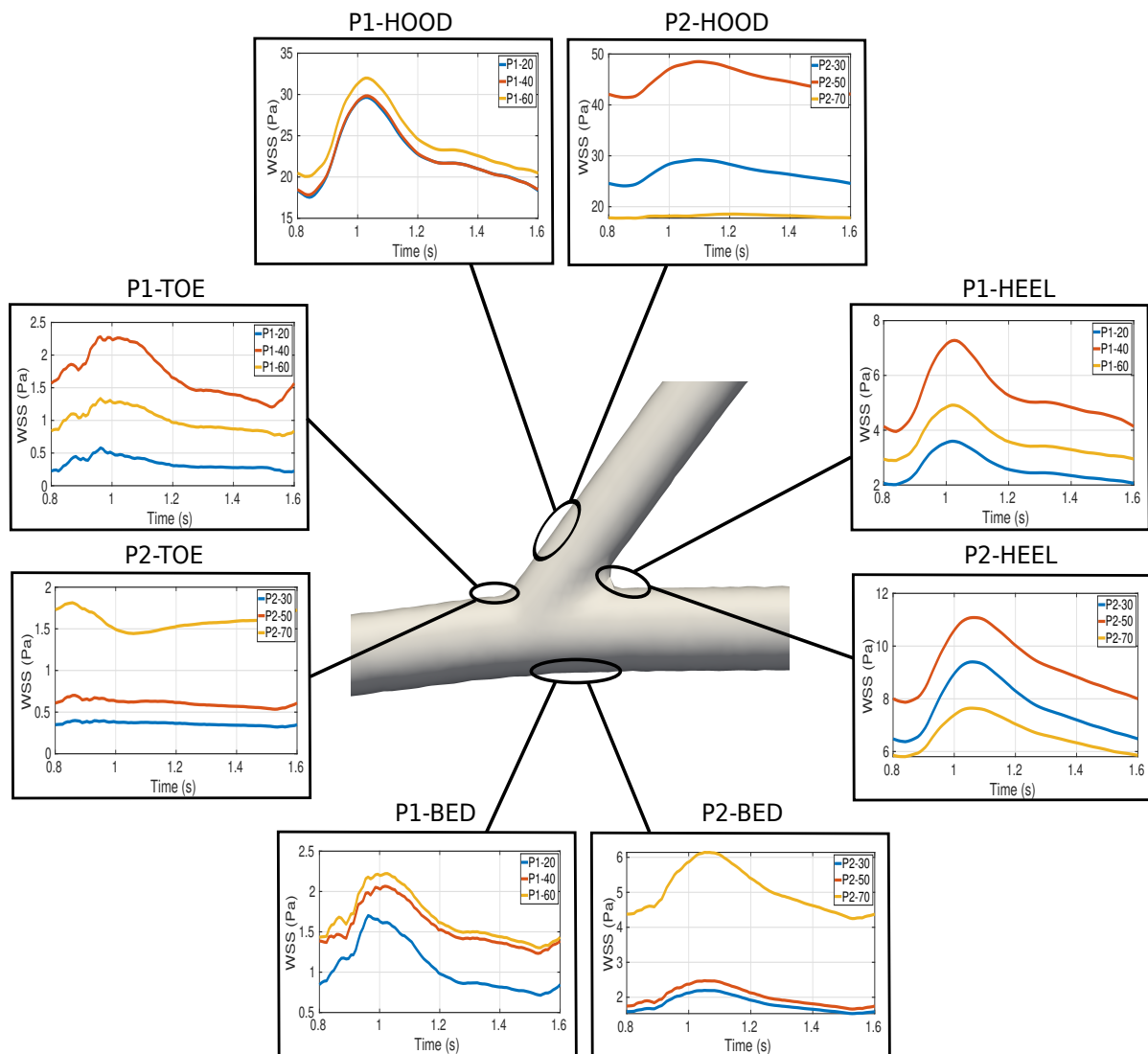
Figure 9: P1 & P2. Space-averaged WSS at the heel, bed, hood and toe of the anastomosis. Notice the different scales in the figures, to highlight significant differences among the anastomosis angles.

in P2 we observe that the increase of the anastomosis angle provokes a strong increase of the displacement in both the anastomosis and juxta-anastomotic regions. In general, since the cephalic vein has a lower compliance, we expect higher displacements, but this is not the case. The reason is that the systemic venous system works with lower pressure (See Fig. 6) and thus the cephalic vein is not forced to the expansion. Focusing on P2, we think that the small diameter of the cephalic vein generates an increase of the velocity field and a decrease of the pressure; therefore, the decrease of the latter causess the diminishing of the displacements (see P2-30 and P2-50). Moreover, since the small diameter of the cephalic vein increases the difficulty of the blood to flow into it, coherently the flow stagnates in the bottom part of the anastomosis region, generating an increase of the displacement, also in the floor of the anastomosis; this is particularly relevant in P2-70. For both P1 and P2, starting from the distal artery, the region of high displacements begins at the toe of the anastomosis where there is a sudden change in the thickness; on the other part, close to the heel, we do not observe any important alteration in the displacement. In literature, our results on the displacement are in agreement with the numerical simulations of [46].

Considering the Von Mises stress (see Fig 11), we observe that the P2 configurations experiment, in all the part of the anastomosis region, twice mechanical stress as much as P1. Since this behaviour is consistent for all the
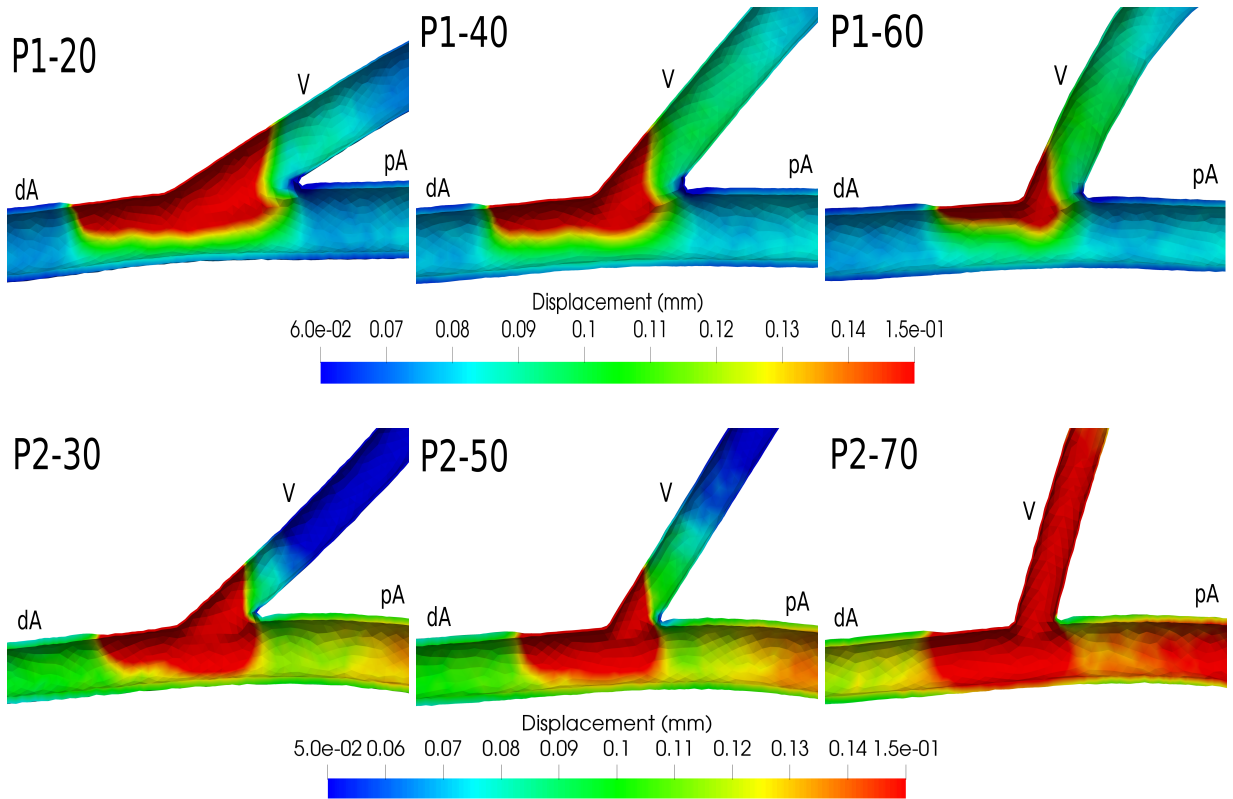
Figure 10: Displacement field at the anastomosis region. First row: P1 configurations at the systolic peak ($t = 1s$). Second row: P2 configurations at the systolic peak ($t = 1s$). Notice the different scales in the figures, to highlight significant differences among the anastomosis angles. pA= proximal artery, dA= distal artery, V= vein.

configurations and parts of the anastomosis region, we think that this increase is due to the small diameter of the cephalic vein. In the case of P1, where the cephalic vein is larger than the radial artery, we note that there are very few differences between P1-40 and P1-60; on the other hand, considering P2, P2-70 seems the worst possibile configuration generating high stress in all the regions. From a mechanical point of view, when the cephalic vein is larger than the radial artery (P1), an increase of the anastomosis angle is not able to modify the stress at the anastomosis region. On the contrary, for small angles of P2, the stress distribution is not affected too much by the change of the angle, but it increases a lot with P2-70. Coherently, the high displacement zones are associated with high value of Von Mises stress as previously seen in other studies [59, 8]

4.5. Final discussion

Our results show that both the diameter of the cephalic vein and the anastomosis angle play a fundamental role for the generation of recirculation regions, abnormal values of WSS, OSI and mechanical stress. For the sake of clearness, we delineate four main critical situations:

a) Low anastomosis angle and large diameter of the cephalic vein (P1-20, P1-40)
b) High anastomosis angle and large diameter of the cephalic vein (P1-60)
c) Low anastomosis angle and small diameter of the cephalic vein (P2-30, P2-50)
d) High anastomosis angle and small diameter of the cephalic vein (P2-70)

When the cephalic vein has a small diameter with respect to that of the radial artery (P2, case c and d above, see Tab. 1), we find:

- Strong increase of the velocity. Generally, high velocity means high WSS which protects against IH, but when the diameter of the cephalic is too small as in this case, the velocity is excessively high and the WSS assume abnormal values. This condition could favor the generation of trombosis;
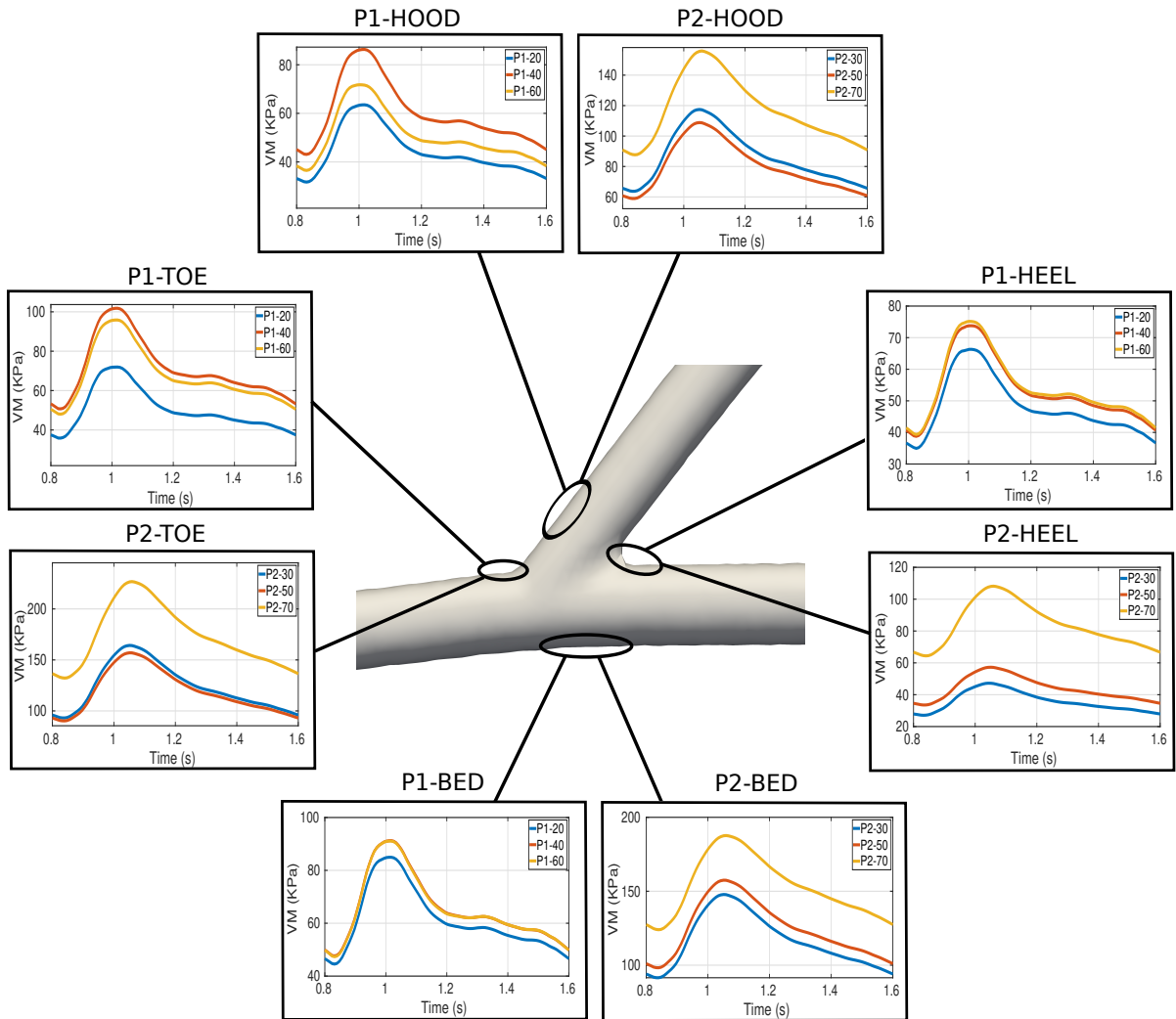
Figure 11: P1 & P2. Space-averaged Von-Mises stress at the heel, bed, hood and toe of the anastomosis. Notice the different scales in the figures, to highlight significant differences among the anastomosis angles.

- The big vortex at the anastomosis region is presented for all the configurations with the same shape and intensity, the anastomosis angle does not have any effect on the blood dynamics;

- Low pressure. The blood does not favour the dilation of the cephalic vein. This condition could not favour the fistula maturation;

- High Von Mises stresses (larger than P1) in all the parts of the anastomosis region.

When the cephalic vein has a larger diameter than the radial artery (P1, case a and b above), the variation of the anastomosis angle influences both the blood dynamics and mechanics of the vessels:

- Case a (P1-20, P1-40):

  - Blood dynamics : Constant presence of a big vortex at the anastomosis region, physiological value of the pressure, unhealthy value of the WSS (too low);

  - Vessel dynamics : The displacements and mechanical stress are lower than Case b in all the part of the anastomosis region.

- Case b (P1-60):
    - Blood dynamics : The presence of the vortex at the anastomosis region is almost absent, physiological values of pressure and WSS are found;
    - Vessel dynamics : Higher displacements and mechanical stresses than Case a.

When the diameter of the cephalic vein is large enough, we confirm that the variation of the anastomosis angles can have a strong effect on the blood dynamics and vessel walls dynamics. In particular, as stated in [62], we confirm that high anastomosis angle (P1-60) are the best in avoiding the recirculation zone and maintaining a healthy WSS. We cannot state the same for P2-70, since we think that the small diameter of the cephalic vein has more influence on the blood dynamics than the change of the anastomosis angle.

It is worth noting that the bifurcation at the distal vein (see Fig.8) is a zone prone for the generation of high values of OSI; in particular, the highest anastomosis angle (P2-70) is the best one in the reduction of OSI.

4.6. Limitations

The main limitations of our work are represented by the boundary conditions. The radial artery and the cephalic vein are not encapsulated in an equal tissue. Since the former lays deeper in the tissues, in a subfascial plane in the wrist, it is more compressed by the external tissues, therefore a further development could be the implementation of the possibility of imposing two different values for the Robin coefficient (α_R). Another improvement could be the choice of a more realistic lumped parameter model for the outlet boundary conditions, in particular, instead of a resistance condition, the three-element Windkessel model can be considered.

Acknowledgments

CRediT authorship contribution statement

References

[1] AHMED, S., ŠUTALO, I. D., AND KAVNOUDIAS, H. Hemodynamics and stress distribution in a cerebral aneurysm partially blocked with coils. In *Proceedings of the 5th International Conference on CFD in the Process Industries CSIRO* (2006), pp. 13–15.

[2] AL-JAISHI, A. A., OLIVER, M. J., THOMAS, S. M., LOK, C. E., ZHANG, J. C., GARG, A. X., KOSA, S. D., QUINN, R. R., AND MOIST, L. M. Patency rates of the arteriovenous fistula for hemodialysis: a systematic review and meta-analysis. *American Journal of Kidney Diseases 63*, 3 (2014), 464–478.

[3] ALAM, N., AND NEWPORT, D. Influence of wall compliance on the flow patterns in a patient-specific brachio-cephalic arterio-venous fistula. *Biomechanics 2*, 2 (2022), 158–173.

[4] AMAYA, R., CANCEL, L. M., AND TARBELL, J. M. Interaction between the stress phase angle (spa) and the oscillatory shear index (osi) affects endothelial cell gene expression. *PLoS One 11*, 11 (2016), e0166569.

[5] ANTIGA, L., PICCINELLI, M., BOTTI, L., ENE-IORDACHE, B., REMUZZI, A., AND STEINMAN, D. A. An image-based modeling framework for patient-specific computational hemodynamics. *Medical & biological engineering & computing 46*, 11 (2008), 1097–1112.

[6] ARMENTANO, R. L., AND CYMBERKNOP, L. J. Mathematical background for mechanical vessel analysis. In *Biomechanical Modeling of the Cardiovascular System*, 2053-2563. IOP Publishing, 2019, pp. 3–1 to 3–24.

[7] BASHAR, K., CLARKE-MOLONEY, M., BURKE, P., KAVANAGH, E., AND WALSH, S. The role of venous diameter in predicting arteriovenous fistula maturation: when not to expect an avf to mature according to pre-operative vein diameter measurements? a best evidence topic. *International Journal of Surgery 15* (2015), 95–99.

[8] BENNATI, L., VERGARA, C., DOMANIN, M., MALLOGGI, C., BISSACCO, D., TRIMARCHI, S., SILANI, V., PARATI, G., AND CASANA, R. A computational fluid–structure interaction study for carotids with different atherosclerotic plaques. *Journal of Biomechanical Engineering 143*, 9 (2021).

[9] BERTAGNA, L., DEPARIS, S., FORMAGGIA, L., FORTI, D., AND VENEZIANI, A. The lifev library: engineering mathematics beyond the proof of concept. arxiv e-prints.

[10] BOZZETTO, M., BRAMBILLA, P., ROTA, S., ENE-IORDACHE, B., SIRONI, S., REMUZZI, G., AND REMUZZI, A. Toward longitudinal studies of hemodynamically induced vessel wall remodeling. *The International Journal of Artificial Organs 41*, 11 (2018), 714–722.

[11] BOZZETTO, M., ENE-IORDACHE, B., AND REMUZZI, A. Transitional flow in the venous side of patient-specific arteriovenous fistulae for hemodialysis. *Annals of biomedical engineering 44*, 8 (2016), 2388–2401.

[12] BOZZETTO, M., SOLIVERI, L., POLONI, S., BRAMBILLA, P., CURTÒ, D., CONDEMI, G. C., CEFALÌ, P., SPINA, I., VILLA, A., CAROLI, A., ET AL. Arteriovenous fistula creation with vasqtm device: A feasibility study to reveal hemodynamic implications. *The Journal of Vascular Access* (2022), 11297298221087160.

[13] BRESCIA, M. J., CIMINO, J. E., APPEL, K., AND HURWICH, B. J. Chronic hemodialysis using venipuncture and a surgically created arteriovenous fistula. *New England Journal of Medicine 275*, 20 (1966), 1089–1092.

[14] CARROLL, G. T., MCGLOUGHLIN, T. M., BURKE, P., EGAN, M., WALLIS, F., AND WALSH, M. T. Wall shear stresses remain elevated in mature arteriovenous fistulas: a case study. *Journal of biomechanical engineering 133*, 2 (2011).

[15] CHANDRA, A., MIX, D., AND VARBLE, N. Hemodynamic study of arteriovenous fistulas for hemodialysis access. *Vascular 21*, 1 (2013), 54–62.

[16] CHEN, X., GAO, Y., LU, B., JIA, X., ZHONG, L., KASSAB, G. S., TAN, W., AND HUO, Y. Hemodynamics in coronary arterial tree of serial stenoses. *PLoS One 11*, 9 (2016), e0163715.

[17] COLLEY, E., CARROLL, J., ANNE, S., SHANNON, T., RAMON, V., AND TRACIE, B. A longitudinal study of the arterio-venous fistula maturation of a single patient over 15 weeks. *Biomechanics and Modeling in Mechanobiology* (2022), 1–16.

[18] COLLEY, E., SIMMONS, A., VARCOE, R., THOMAS, S., AND BARBER, T. Arteriovenous fistula maturation and the influence of fluid dynamics. *Proceedings of the Institution of Mechanical Engineers, Part H: Journal of Engineering in Medicine 234*, 11 (2020), 1197–1208.

[19] DE VILLIERS, A., MCBRIDE, A., REDDY, B., FRANZ, T., AND SPOTTISWOODE, B. A validated patient-specific fsi model for vascular access in haemodialysis. *Biomechanics and modeling in mechanobiology 17*, 2 (2018), 479–497.

[20] DECORATO, I., KHARBOUTLY, Z., LEGALLAIS, C., AND SALSAC, A.-V. Comparison of two endovascular treatments of a stenosed arteriovenous fistula: balloon-angioplasty with and without stenting. *The International Journal of Artificial Organs 37*, 10 (2014), 763–772.

[21] DECORATO, I., KHARBOUTLY, Z., VASSALLO, T., PENROSE, J., LEGALLAIS, C., AND SALSAC, A.-V. Numerical simulation of the fluid structure interactions in a compliant patient-specific arteriovenous fistula. *International journal for numerical methods in biomedical engineering 30*, 2 (2014), 143–159.

[22] DEPARIS, S., FORTI, D., GERVASIO, P., AND QUARTERONI, A. Internodes: an accurate interpolation-based method for coupling the galerkin solutions of pdes on subdomains featuring non-conforming interfaces. *Computers & Fluids 141* (2016), 22–41.

[23] DEPARIS, S., FORTI, D., GRANDPERRIN, G., AND QUARTERONI, A. Facsi: A block parallel preconditioner for fluid–structure interaction in hemodynamics. *Journal of Computational Physics 327* (2016), 700–718.

[24] DEPARIS, S., FORTI, D., AND QUARTERONI, A. A fluid–structure interaction algorithm using radial basis function interpolation between non-conforming interfaces. *Advances in Computational Fluid-Structure Interaction and Flow Simulation: New Methods and Challenging Computations* (2016), 439.

[25] ENE-IORDACHE, B., CATTANEO, L., DUBINI, G., AND REMUZZI, A. Effect of anastomosis angle on the localization of disturbed flow in 'side-to-end' fistulae for haemodialysis access. *Nephrology Dialysis Transplantation 28*, 4 (2013), 997–1005.

[26] ENE-IORDACHE, B., AND REMUZZI, A. Disturbed flow in radial-cephalic arteriovenous fistulae for haemodialysis: low and oscillating shear stress locates the sites of stenosis. *Nephrology Dialysis Transplantation 27*, 1 (2012), 358–368.

[27] ENE-IORDACHE, B., SEMPERBONI, C., DUBINI, G., AND REMUZZI, A. Disturbed flow in a patient-specific arteriovenous fistula for hemodialysis: multidirectional and reciprocating near-wall flow patterns. *Journal of biomechanics 48*, 10 (2015), 2195–2200.

[28] FAHRTASH, F., KAIRAITIS, L., GRUENEWALD, S., SPICER, T., SIDRAK, H., FLETCHER, J., ALLEN, R., AND SWINNEN, J. Defining a significant stenosis in an autologous radio-cephalic arteriovenous fistula for hemodialysis. In *Seminars in Dialysis* (2011), vol. 24, Wiley Online Library, pp. 231–238.

[29] FEDELE, M., AND QUARTERONI, A. Polygonal surface processing and mesh generation tools for the numerical simulation of the cardiac function. *International Journal for Numerical Methods in Biomedical Engineering 37*, 4 (2021), e3435.

[30] FINLAY, D. E., LONGLEY, D. G., FOSHAGER, M. C., AND LETOURNEAU, J. G. Duplex and color doppler sonography of hemodialysis arteriovenous fistulas and grafts. *Radiographics 13*, 5 (1993), 983–989.

[31] FORMAGGIA, L., QUARTERONI, A., AND VENEZIANI, A. *Cardiovascular Mathematics: Modeling and simulation of the circulatory system*, vol. 1. Springer Science & Business Media, 2010.

[32] FORMAGGIA, L., AND VERGARA, C. Prescription of general defective boundary conditions in fluid-dynamics. *Milan Journal of Mathematics 80*, 2 (2012), 333–350.

[33] FORTI, D., BUKAC, M., QUAINI, A., CANIC, S., AND DEPARIS, S. A monolithic approach to fluid–composite structure interaction. *Journal of Scientific Computing 72*, 1 (2017), 396–421.

[34] FORTI, D., AND DEDÈ, L. Semi-implicit bdf time discretization of the navier–stokes equations with vms-les modeling in a high performance computing framework. *Computers & Fluids 117* (2015), 168–182.

[35] GAMEIRO, J., AND IBEAS, J. Factors affecting arteriovenous fistula dysfunction: a narrative review. *The Journal of Vascular Access 21*, 2 (2020), 134–147.

[36] GEUZAINE, C., AND REMACLE, J.-F. Gmsh: A 3-d finite element mesh generator with built-in pre-and post-processing facilities. *International journal for numerical methods in engineering 79*, 11 (2009), 1309–1331.

[37] GUESS, W., REDDY, B., MCBRIDE, A., SPOTTISWOODE, B., DOWNS, J., AND FRANZ, T. Fluid-structure interaction modelling and stabilisation of a patient-specific arteriovenous access fistula.

[38] KHEDA, M. F., BRENNER, L. E., PATEL, M. J., WYNN, J. J., WHITE, J. J., PRISANT, L. M., JONES, S. A., AND PAULSON, W. D. Influence of arterial elasticity and vessel dilatation on arteriovenous fistula maturation: a prospective cohort study. *Nephrology Dialysis Transplantation 25*, 2 (2010), 525–531.

[39] KIM, Y. O., CHOI, Y. J., KIM, J. I., KIM, Y. S., KIM, B. S., PARK, C. W., SONG, H. C., YOON, S. A., CHANG, Y. S., AND BANG, B. K. The impact of intima-media thickness of radial artery on early failure of radiocephalic arteriovenous fistula in hemodialysis patients. *Journal of Korean medical science 21*, 2 (2006), 284–289.

[40] KORDZADEH, A., CHUNG, J., AND PANAYIOTOPOULOS, Y. P. Cephalic vein and radial artery diameter in formation of radiocephalic arteriovenous fistula: a systematic review. *The journal of vascular access 16*, 6 (2015), 506–511.

[41] LANCELLOTTI, R. M., VERGARA, C., VALDETTARO, L., BOSE, S., AND QUARTERONI, A. Large eddy simulations for blood dynamics in realistic stenotic carotids. *International journal for numerical methods in biomedical engineering 33*, 11 (2017), e2868.

[42] LAURENT, S., GIRERD, X., MOURAD, J.-J., LACOLLEY, P., BECK, L., BOUTOUYRIE, P., MIGNOT, J.-P., AND SAFAR, M. Elastic modulus of the radial artery wall material is not increased in patients with essential hypertension. *Arteriosclerosis and thrombosis: a journal of vascular biology 14*, 7 (1994), 1223–1231.

[43] LIU, J., YANG, W., LAN, I. S., AND MARSDEN, A. L. Fluid-structure interaction modeling of blood flow in the pulmonary arteries using the unified continuum and variational multiscale formulation. *Mechanics research communications 107* (2020), 103556.

[44] LONG, C., HSU, M.-C., BAZILEVS, Y., FEINSTEIN, J., AND MARSDEN, A. Fluid–structure interaction simulations of the fontan procedure using variable wall properties. *International journal for numerical methods in biomedical engineering 28*, 5 (2012), 513–527.

[45] MATLAB. *version R2022a*. The MathWorks Inc., Natick, Massachusetts, 2022.

[46] MCGAH, P. M., LEOTTA, D. F., BEACH, K. W., AND ALISEDA, A. Effects of wall distensibility in hemodynamic simulations of an arteriovenous fistula. *Biomechanics and modeling in mechanobiology 13*, 3 (2014), 679–695.

[47] MOUSA, A. Y., DEARING, D. D., AND ABURAHMA, A. F. Radiocephalic fistula: review and update. *Annals of Vascular Surgery 27*, 3 (2013), 370–378.

[48] NATIONAL INSTITUTES OF HEALTH, N. I. O. D., DIGESTIVE, AND DISEASES, K. 2021 usrds annual data report: Epidemiology of kidney disease in the united states, 2021.

[49] NOBILE, F., POZZOLI, M., AND VERGARA, C. Time accurate partitioned algorithms for the solution of fluid–structure interaction problems in haemodynamics. *Computers & Fluids 86* (2013), 470–482.

[50] OCHSNER JR, A., COLP JR, R., AND BURCH, G. Normal blood pressure in the superficial venous system of man at rest in the supine position. *Circulation 3*, 5 (1951), 674–680.

[51] PICCINELLI, M., VERGARA, C., ANTIGA, L., FORZENIGO, L., BIONDETTI, P., AND DOMANIN, M. Impact of hemodynamics on lumen boundary displacements in abdominal aortic aneurysms by means of dynamic computed tomography and computational fluid dynamics. *Biomechanics and modeling in mechanobiology 12*, 6 (2013), 1263–1276.

[52] QUARTERONI, A., MANZONI, A., AND VERGARA, C. The cardiovascular system: mathematical modelling, numerical algorithms and clinical applications. *Acta Numerica 26* (2017), 365–590.

[53] QUARTERONI, A., VENEZIANI, A., AND VERGARA, C. Geometric multiscale modeling of the cardiovascular system, between theory and practice. *Computer Methods in Applied Mechanics and Engineering 302* (2016), 193–252.

[54] QUENCER, K. B., AND ARICI, M. Arteriovenous fistulas and their characteristic sites of stenosis. *American Journal of Roentgenology 205*, 4 (2015), 726–734.

[55] QUICKEN, S., DE BRUIN, Y., MEES, B., TORDOIR, J., DELHAAS, T., AND HUBERTS, W. Computational study on the haemodynamic and mechanical performance of electrospun polyurethane dialysis grafts. *Biomechanics and modeling in mechanobiology 19*, 2 (2020), 713–722.

[56] ROBBIN, M. L., GREENE, T., CHEUNG, A. K., ALLON, M., BERCELI, S. A., KAUFMAN, J. S., ALLEN, M., IMREY, P. B., RADEVA, M. K., SHIU, Y.-T., ET AL. Arteriovenous fistula development in the first 6 weeks after creation. *Radiology 279*, 2 (2016), 620–629.

[57] SADEGHI, M., SHIRANI, E., TAFAZZOLI-SHADPOUR, M., AND SAMAEE, M. The effects of stenosis severity on the hemodynamic parameters—assessment of the correlation between stress phase angle and wall shear stress. *Journal of biomechanics 44*, 15 (2011), 2614–2626.

[58] SCHNELL, W. Westergaard, hm-theory of elasticity and plasticity, 1966.

[59] SHEMBEKAR, S. N., ZODPE, D., AND PADOLE, P. M. Fluid-structure interaction of pulsatile flow within the flexible wall radio-cephalic arteriovenous fistula. *Available at SSRN 4044568*.

[60] SIVANESAN, S., HOW, T. V., AND BAKRAN, A. Sites of stenosis in av fistulae for haemodialysis access. *Nephrology, dialysis, transplantation: official publication of the European Dialysis and Transplant Association-European Renal Association 14*, 1 (1999), 118–120.

[61] SKACEL, P., AND BURSA, J. Poisson's ratio and compressibility of arterial wall–improved experimental data reject auxetic behaviour. *Journal of the Mechanical Behavior of Biomedical Materials 131* (2022), 105229.

[62] STELLA, S., VERGARA, C., GIOVANNACCI, L., QUARTERONI, A., AND PROUSE, G. Assessing the disturbed flow and the transition to turbulence in the arteriovenous fistula. *Journal of biomechanical engineering 141*, 10 (2019).

[63] TEZDUYAR, T. E. Stabilized finite element formulations for incompressible flow computations. *Advances in applied mechanics 28* (1991), 1–44.

[64] VAZQUEZ-PADRON, R. I., DUQUE, J. C., TABBARA, M., SALMAN, L. H., AND MARTINEZ, L. Intimal hyperplasia and arteriovenous fistula failure: Looking beyond size differences. *Kidney360 2*, 8 (2021), 1360.

[65] YANG, Y. *Analysis of personalized mechano-bio-faithful radio-cephalic arteriovenous Fistula*. PhD thesis, Université de Lyon, 2021.

[66] ZHANG, F., LI, Y., WANG, T., TAO, J., ZHU, J., WEI, M., MO, L., LI, X., WANG, Y., AND CHENG, Y. Influence of cephalic vein dilation on arteriovenous fistula maturation in patients with small cephalic veins. *Medicine 99*, 1 (2020).

MOX Technical Reports, last issues

Dipartimento di Matematica

Politecnico di Milano, Via Bonardi 9 - 20133 Milano (Italy)

17/2023   Savin, M.S.; Cavinato, L.; Costa, G.; Fiz, F.; Torzilli, G.; Vigano', L.; Ieva, F.

   Distant supervision for imaging-based cancer sub-typing in Intrahepatic Cholangiocarcinoma

18/2023   Marcinno', F.; Vergara, C.; Giovannacci, L.; Quarteroni, A.; Prouse, G.

   Computational fluid-structure interaction analysis of the end-to-side radio-cephalic arteriovenous fistula

15/2023   Ragni, A.; Masci, C.; Ieva, F.; Paganoni, A. M.

   Clustering Hierarchies via a Semi-Parametric Generalized Linear Mixed Model: a statistical significance-based approach

   Bertoletti, A.; Cannistrà, M.; Diaz Lema, M.; Masci, C.; Mergoni, A.;Rossi, L.; Soncin, M.

   The Determinants of Mathematics Achievement: A Gender Perspective Using Multilevel Random Forest

13/2023   Masci, C.; Cannistrà, M.; Mussida, P.

   Modelling time-to-dropout via Shared Frailty Cox Models. A trade-off between accurate and early predictions

11/2023   Gatti, F.; Perotto, S.; de Falco, C.; Formaggia, L.

   A positivity-preserving well-balanced numerical scheme for the simulation of fast landslides with efficient time stepping

10/2023   Corti, M.; Antonietti, P.F.; Bonizzoni, F.; Dede', L., Quarteroni, A.

   Discontinuous Galerkin Methods for Fisher-Kolmogorov Equation with Application to Alpha-Synuclein Spreading in Parkinson's Disease

09/2023   Buchwald, S.; Ciaramella, G.; Salomon, J.

   Gauss-Newton oriented greedy algorithms for the reconstruction of operators in nonlinear dynamics

08/2023   Bonizzoni, F.; Hu, K.; Kanschat, G.; Sap, D.

   Discrete tensor product BGG sequences: splines and finite elements

06/2023   Artoni, A.; Antonietti, P. F.; Mazzieri, I.; Parolini, N.; Rocchi, D.

   A segregated finite volume - spectral element method for aeroacoustic problems